International Journal of Heat and Mass Transfer 211 (2023) 124203

Contents lists available at ScienceDirect

International Journal of Heat and Mass Transfer

journal homepage: www.elsevier.com/locate/hmt

A comprehensive hybrid transient CFD-thermal resistance model for automobile thermoelectric generators

Ding Luo[a,*], Yuying Yan[d], Wei-Hsin Chen[e,f,g], Xuelin Yang[a], Hao Chen[h], Bingyang Cao[c,*], Yulong Zhao[b,*]

[a] College of Electrical Engineering & New Energy, China Three Gorges University, Yichang, China
[b] Hebei Key Laboratory of Thermal Science and Energy Clean Utilization, Hebei University of Technology, Tianjin 300401, China
[c] Department of Engineering Mechanics, Key Laboratory for Thermal Science and Power Engineering of Ministry of Education, Tsinghua University, Beijing 100084, China
[d] Faculty of Engineering, University of Nottingham, University Park, Nottingham, UK
[e] Department of Aeronautics and Astronautics, National Cheng Kung University, Tainan 701, Taiwan
[f] Research Center for Smart Sustainable Circular Economy, Tunghai University, Taichung 407, Taiwan
[g] Department of Mechanical Engineering, National Chin-Yi University of Technology, Taichung 411, Taiwan
[h] Shaanxi Key Laboratory of New Transportation Energy and Automotive Energy Saving, Chang'an University, Xi'an, China

ARTICLE INFO

Article history:
Received 4 December 2022
Revised 19 February 2023
Accepted 13 April 2023

Keywords:
Dynamic behaviour
Thermoelectric generator
CFD
Thermal resistance
Transient model

ABSTRACT

This paper proposes a comprehensive hybrid transient CFD-thermal resistance model to predict the dynamic behaviour of an automobile thermoelectric generator (ATEG) system. The model takes into account the temperature dependences, the topological connection of thermoelectric modules, and the dynamic characteristics, which has the merits of high accuracy and short computational time. The dynamic behaviour of the ATEG system is determined and thoroughly examined using the transient exhaust heat as the heat source input. According to the transient model results, the dynamic output power of the ATEG system keeps the same variation trend with the exhaust temperature, but the variation of output power is more stable. Under the whole driving cycle, the mean power and efficiency of the 1/4 ATEG system are 8.91 W and 3.39% respectively, which are 3.39% lower and 47.52% higher than those expected by steady-state analysis. Beside, the model is validated experimentally, and the mean deviations of the output voltage and outlet air temperature are 7.70% and 1.12% respectively. This model is convenient to evaluate the behaviour of the ATEG system under different topological connections and gives a fresh tool for assessing the dynamic behaviour of ATEG systems.

1. Introduction

For conventional automobiles, the heat contained in exhaust accounts for approximately 1/3 of the total energy produced by burning fossil fuels [1]. This waste heat can be recycled and turned into energy by the automobile thermoelectric generator (ATEG) system, so as to reduce the consumption of oils [2–4]. In order to evaluate the profit and fuel-saving brought by the ATEG system to vehicles, theoretical models are vital to predict its output performance. When the vehicle is running in a transient driving cycle, the exhaust parameters will change all the time, resulting in a change of behaviour of the ATEG system. Accordingly, how to accurately predict the dynamic behaviour of the ATEG system is one of the engineering issues highly required to be solved.

A typical ATEG system is comprised of a heat exchanger, a set of thermoelectric modules (TEMs), and heat sinks [5]. To accurately evaluate the performance of TEMs, the heat and mass transfer of fluid regions and solid regions, and the thermal-electric conversion of TEMs should be taken into account [6]. In recent years, several models for ATEG systems have been developed, including computational fluid dynamics (CFD) models [7], thermal resistance models [8], and hydraulic-thermoelectric numerical models [9]. CFD models could accurately compute the conjugate heat transfer and are widely used to assess the thermodynamic behaviour of ATEG systems [10]. Under specific working temperatures, the output performance of TEMs can be calculated by a thermal resistance model [11], and further, the behaviour of ATEG systems could be obtained by considering the convection between fluid regions and solid regions. In recent studies [12,13], hydraulic-thermoelectric multi-

* Corresponding authors.
E-mail addresses: Ding_L@outlook.com (D. Luo), caoby@tsinghua.edu.cn (B. Cao), zhaoyulong@hebut.edu.cn (Y. Zhao).

https://doi.org/10.1016/j.ijheatmasstransfer.2023.124203
0017-9310/

Nomenclature

Symbols

A	area, mm^2
c	specific heat, $J \cdot kg^{-1} \cdot K^{-1}$
H	height, mm
h	heat transfer coefficient, $W \cdot m^{-2} \cdot K^{-1}$
I	output current, A
k	turbulent kinetic energy, $m^2 \cdot s^{-2}$
$\dot{m}$	mass flow rate, $g \cdot s^{-1}$
N	number of thermoelectric couples
p	pressure, Pa
P	power, W
Q	heat, W
R	resistance, Ω or $K \cdot W^{-1}$
T	temperature, K
t	time, s
U	output voltage, V
$\vec{v}$	velocity vector, $m \cdot s^{-1}$

Greek symbols

ρ	density, $kg \cdot m^{-3}$
μ	dynamic viscosity, $Pa \cdot s$
λ	thermal conductivity, $W \cdot m^{-1} \cdot K^{-1}$
ε	turbulent dissipation rate, $m^2 \cdot s^{-3}$
α	Seebeck coefficient, $\mu V \cdot K^{-1}$
σ^{-1}	electrical resistivity, $\Omega \cdot m$
η	conversion efficiency

Subscripts

c	cold side
cce	cold-side ceramic plate
cleg	cold side of thermoelectric legs
co	copper
en	environment
ex	exhaust gas
h	hot side
hce	hot-side ceramic plate
hleg	hot side of thermoelectric legs
i	ith thermoelectric module, $i = 1, 2, 3, 4$
in	internal resistance
L	length or load resistance
leg	thermoelectric legs
n	n-type thermoelectric legs
p	p-type thermoelectric legs
pn	thermoelectric couples

Abbreviations

ATEG	automotive thermoelectric generator
CFD	computational fluid dynamics
HWFET	highway fuel economy test
TEM	thermoelectric module

physics numerical models have been created by combining the CFD model and thermal-electric numerical model; In comparison to the CFD and thermal resistance models, this model exhibits higher reasonability and accuracy. Most of the proposed models, however, do not take into account dynamic performance of ATEG systems since they are steady-state models. It is of great significance to establish a reasonable transient model.

Wang et al. [14] used the exhaust heat as boundary conditions of the CFD model to analyse the thermodynamic performance of the ATEG system under different heat exchanger structures and TEM distributions. Their findings showed that the heat exchanger with cylindrical grooves outperformed other heat exchangers. Nithyanandam and Mahajan [15] integrated the metal foam into the ATEG system to enhance heat transfer between the heat exchanger and exhaust gas, and the influence of different pore densities on the behaviour of the ATEG system under various inlet conditions of the exhaust gas was studied by using the steady-state CFD model. It is not possible to obtain the electrical output of the ATEG system with a CFD model, but the temperature distributions on both sides of the TEMs can be obtained. After that, based on the mean surface temperatures, it is possible to compute the output of the ATEG system by using a fitted method [16,17] or a simple calculation [18]. The transient CFD model has been widely used in other scenarios, such as solar still [19], combustion [20], and conjugate heat transfer [21]. However, the transient CFD modeling for the ATEG system has not been reported yet. It is completely feasible to carry out transient CFD simulations of the ATEG system by introducing a transient term into the steady-state CFD model and taking the dynamic exhaust heat as transient boundary conditions, and it is more consistent with the fact that the exhaust parameters change with vehicle speed.

The thermal resistance model, derived from a thermal resistance network, features the advantage of reducing computing time. Generally, the thermal resistance model is calculated assuming uniform surface temperatures, ignoring environmental heat loss and Thomson heat in thermoelectric legs [22]. Zhang et al. [23] used a thermal resistance model to analyse the power and efficiency of a cascading TEM for waste heat recovery from solid oxide fuel cells; A two-stage TEM was optimized and analyzed using the thermal resistance model by Liang et al. [24]. Through a comparison of different models, Fraisse et al. [25] found that the thermal-electric numerical model and thermal resistance model predict similar performance for TEM output performance, because the heat loss and Thomson heat play an insignificant role in the overall heat transfer of the TEM. Furthermore, by introducing the convective thermal resistance in fluid areas and conductive thermal resistances of heat exchangers into the thermal resistance model of TEMs, Marvão et al. [26] and Vale et al. [27] developed a comprehensive thermal resistance model for the ATEG system and used it to evaluate the behaviour of the ATEG system under various structural parameters. Also, Gou et al. [28] and Lan et al. [29] have extended the steady-state thermal resistance model of the ATEG system to a transient state, and the dynamic behaviour of the ATEG system was studied under transient exhaust heat input using the proposed transient thermal resistance model. However, it has been shown that the thermal resistance model of the ATEG system predicts unreasonable output performance, and its accuracy is influenced by exhaust parameters [30]. In contrast to the ATEG thermal resistance model, the TEM one only ignores heat loss between the TEM and the environment, making it more accurate. Nevertheless, an empirical formula is used to represent the turbulence flow in fluid areas, but the heat loss of heat exchangers is not included in the thermal resistance model of the ATEG system, thus resulting in a non-negligible error, especially for the dynamic performance analysis.

Compared with CFD models and thermal resistance models, the hydraulic-thermoelectric multiphysics model features the highest reasonability, because the coupling among fluid, thermal, and electric fields are completely considered. In Ref. [13], a steady-state hydraulic-thermoelectric multiphysics model was developed to evaluate the behaviour of ATEG systems with longitudinal vortex generators; In the model, the complete TEM structure with multiple thermoelectric couples was simplified to a TEM structure with only one thermoelectric couple. Using a steady-state hydraulic-thermoelectric multiphysics model, Yan et al. [31] studied the influence of heat exchange shapes on ATEG performance, in which the structure of heat sinks was absent and replaced by a fixed cold-side temperature. Luo et al. [32] established a steady-state hydraulic-thermoelectric multiphysics model for an ATEG system

with only one TEM, in which the complete structure was considered, but the thermal-electric coupling field and the fluid-thermal coupling field were calculated separately. In their recent study [33], a transient hydraulic-thermoelectric multiphysics model for a simplified ATEG system was established to predict its dynamic performance under transient driving cycles; During simulations, the required time for the simplified ATEG system with only one TEM was 7 days, which has already consumed tremendous computing resources and time, not to mention a complete structure.

As mentioned above, a precise transient model is necessary to assess the dynamic behaviour of ATEG systems under actual vehicle driving conditions. The current steady-state CFD model could be extended to the transient state and used to simulate the transient heat and mass transfer of the ATEG system, but cannot obtain the electrical performance of ATEG systems. The thermal resistance model of the TEM can accurately calculate the electrical output of TEMs at specific working temperatures, but when the thermal resistance model is applied to ATEG systems, the error was not acceptable. Moreover, the thermal resistance model in previous studies [34,35] usually focused on the calculation of a single TEM, ignoring the topological connection between different TEMs. In Ref. [36], recent advances in modeling from one-dimensional to three-dimensional and from steady-state to transient were provided in detail, including the transient thermal resistance model [29] and the transient hydraulic-thermoelectric multiphysics model [33]. However, the transient thermal resistance model features large errors due to the neglect of turbulence flow, and the transient hydraulic-thermoelectric multiphysics model consumes a lot of calculation time and resources. To address these issues, this study endeavours to develop a comprehensive transient model of the ATEG system by fully utilizing the advantages of the CFD model and the thermal resistance model.

In the present work, a complete hybrid transient CFD-thermal resistance model is developed to study the dynamic behaviour of ATEG systems. This model considers the temperature dependences, the topological connection of TEMs, and the transient conjugate heat transfer, which provides a brand new tool for evaluating the dynamic behaviour of the ATEG system. The structure of this work is: Section 2 introduces the research objectives, including the ATEG system used and the vehicle used to generate transient exhaust heat; Section 3 gives details about the hybrid transient CFD-thermal resistance model; Section 4 introduces the experimental setup and compares the model results with the experimental results; Section 5 gives detailed analysis and discussion about the dynamic performance of the ATEG system; Finally, the key findings are summarized in Section 6.

2. Research objective

An automobile thermoelectric generator (ATEG) system is designed to reuse the exhaust heat from a heavy truck, as shown in Fig. 1. Here, the heavy truck model is built on the platform of ADVISOR. The heavy truck with a total mass of 9068 kg is driven by a 7.2 L diesel engine with a maximum engine power of 206 kW. In general, the ATEG system is installed between the exhaust after-treatment device and the muffler. Therefore, the transient exhaust heat at this position is extracted from the simulation results of ADVISOR. To match the exhaust pipe of the heavy truck, the inlet and outlet diameters of the heat exchanger are designed as 50 mm. The size of the main part of the heat exchanger is 212×110×70 (L×W×H) mm^3. To effectively extract heat from the exhaust gas, twenty plate fins with the size of 200×2×20 (L×W×H) mm^3 are evenly distributed on the two internal hot sides of the heat exchanger. Also, sixteen Bi_2Te_3-based commercial TEMs (TEG-127,020, P&N technology, China) are evenly attached on the two external hot sides of the heat exchanger. One TEM is comprised of two ceramic plates (44×40×0.8 (L×W×H) mm^3 for the hot-side one and 40×40×0.8 (L×W×H) mm^3 for the cold-side one), 256 copper conducting strips (3.8×1.4×0.35 (L×W×H) mm^3), 128 p-type thermoelectric legs (1.4×1.4×1 (L×W×H) mm^3), and 128 n-type thermoelectric legs (1.4×1.4×1 (L×W×H) mm^3). To effectively dissipate the heat and provide a cooling source for TEMs, four heat sinks are applied on the two sides of the ATEG system, and each heat sink is matched with four TEMs.

The transient CFD simulation of the whole ATEG system will consume a lot of computing power and time. Considering that the geometric structure of the ATEG system is completely symmetrical, taking 1/4 of the ATEG system as the object, the dynamic behaviour of the ATEG system is analyzed in detail. Beside, in CFD simulations, the function of TEMs is only as a heat conduction unit. For this reason, the whole TEM is simplified as a cuboid (40×40×3.3 (L×W×H) mm^3) to replace the complex structure of TEMs, and this simplification barely affects the results. To ensure the accuracy of this geometric simplification, the equivalent thermal conductivity considering temperature dependence in [37] is adopted for the simplified TEM.

Furthermore, the higher the thermal conductivity of the heat exchanger and heat sinks is, the greater the temperature difference of TEMs will be. Therefore, the heat exchanger and heat sinks are made of 6063 aluminium alloy. Dry air is used as the heat source for the ATEG system, and water as the cooling source. Detailed material parameters of the ATEG system are tabulated in Table 1, where the thermal conductivity of copper takes into account the thermal resistance of solder layers [37].

3. The comprehensive hybrid transient CFD-thermal resistance model

The comprehensive hybrid transient CFD-thermal resistance model includes two sub-models: the transient CFD model and the transient thermal resistance model. To solve this hybrid transient model, the following preconditions are made:

- The Thomson effect is neglected because of its tiny influence [38].
- The surface temperature of TEMs is assumed to be uniform when solving the thermal resistance model.
- The heat radiation is omitted.
- The contact thermal resistance between different structures is omitted because the thermal grease is evenly applied on the two sides of TEMs, and the whole ATEG system is clamped together with enough pressure. Through the preliminary calculation, the error caused by this ignorance is less than 0.26%, which barely affects the overall performance of the ATEG system.

3.1. Principles of the model

The transient CFD model was widely adopted to conduct dynamic thermodynamic performance analysis in other fields. Considering the dynamic behaviour of the ATEG system for automobile exhaust heat recovery, the transient CFD model is more reasonable than a steady one and more fit in actual situations. The basic equations of the transient CFD model are:

$$\frac{\partial \rho}{\partial t} + \nabla \cdot (\rho \vec{v}) = 0 \tag{1}$$

$$\frac{\partial}{\partial t}(\rho \vec{v}) + \nabla \cdot (\rho \vec{v}\vec{v}) = -\nabla p + \nabla \cdot \left[\mu\left(\nabla \vec{v} + \nabla \vec{v}^T\right)\right] \tag{2}$$

$$\rho c \frac{\partial T}{\partial t} + \rho c \vec{v} \cdot \nabla T - \nabla \cdot (\lambda \nabla T) = 0 \tag{3}$$

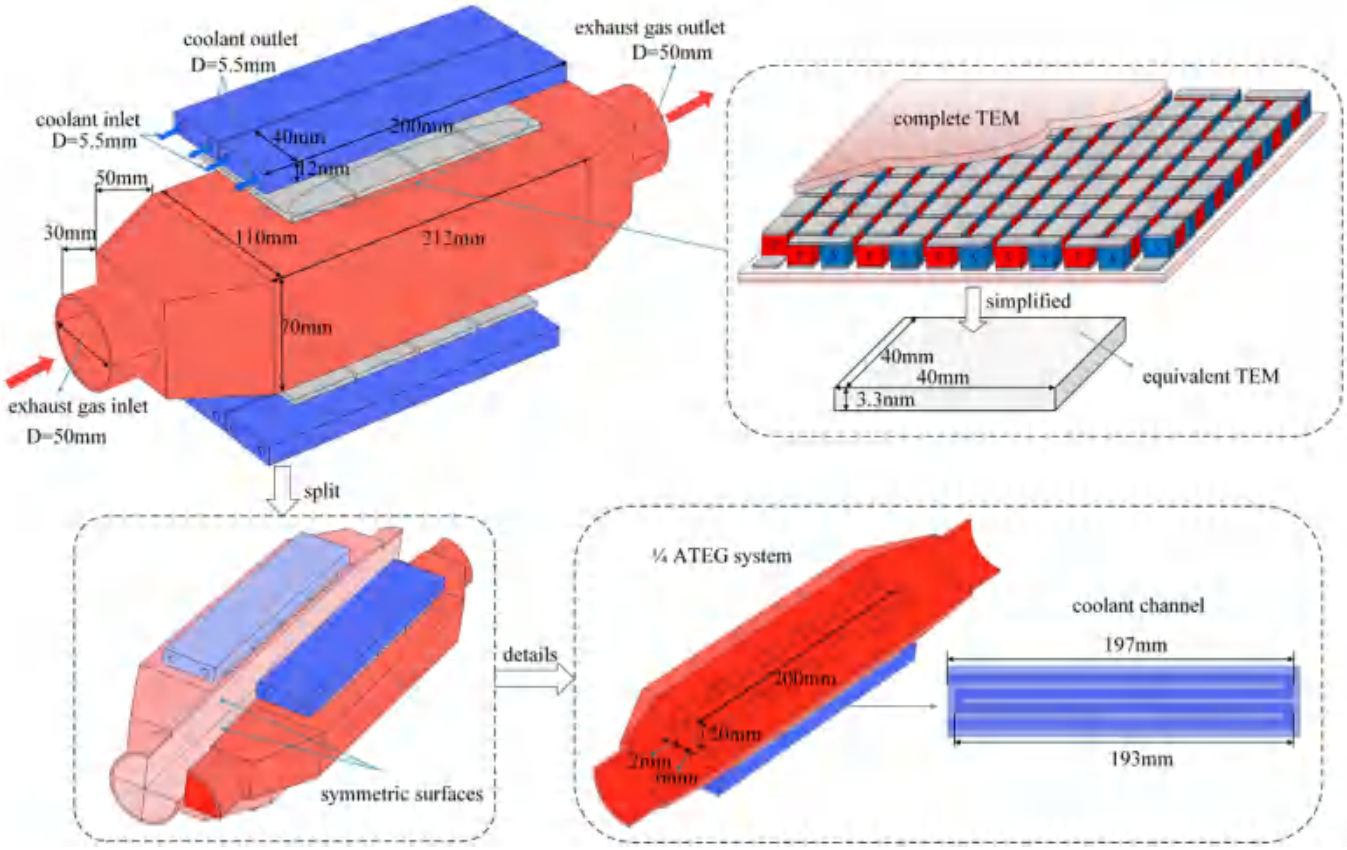

Fig. 1. Structure of the ATEG system.

Table 1
Material properties of the automobile thermoelectric generator system.

Component name	Parameter	Value	Unit
Heat exchanger and heat sinks	thermal conductivity	201	$W\cdot m^{-1}\cdot K^{-1}$
	specific heat	871	$J\cdot kg^{-1}\cdot K^{-1}$
Ceramic plates	thermal conductivity	22	$W\cdot m^{-1}\cdot K^{-1}$
	specific heat	850	$J\cdot kg^{-1}\cdot K^{-1}$
Copper conducting strips	thermal conductivity	165.64	$W\cdot m^{-1}\cdot K^{-1}$
	electrical resistivity	1.75×10^{-8}	ohm·m
	specific heat	381	$J\cdot kg^{-1}\cdot K^{-1}$
p-type thermoelectric legs	thermal conductivity	$-3.05948\times10^{-9}T^4+4.56781\times10^{-6}T^3$ $-2.51621\times10^{-3}T^2+0.61074T-53.98632$	$W\cdot m^{-1}\cdot K^{-1}$
	electrical resistivity	$-3.08802\times10^{-9}T^4+4.56531\times10^{-6}T^3$ $-2.58541\times10^{-3}T^2+0.65579T-60.58804$	10^{-5}ohm·m
	Seebeck coefficient	$-1.80268\times10^{-7}T^4+3.23632\times10^{-4}T^3$ $-0.21537T^2+62.97444T-6616.56781$	$\mu V\cdot K^{-1}$
	specific heat	188	$J\cdot kg^{-1}\cdot K^{-1}$
n-type thermoelectric legs	thermal conductivity	$-3.05948\times10^{-9}T^4+4.56781\times10^{-6}T^3$ $-2.51621\times10^{-3}T^2+0.61074T-53.98632$	$W\cdot m^{-1}\cdot K^{-1}$
	electrical resistivity	$-3.08802\times10^{-9}T^4+4.56531\times10^{-6}T^3$ $-2.58541\times10^{-3}T^2+0.65579T-60.58804$	10^{-5}ohm·m
	Seebeck coefficient	$1.80268\times10^{-7}T^4-3.23632\times10^{-4}T^3$ $+0.21537T^2-62.97444T+6616.56781$	$\mu V\cdot K^{-1}$
	specific heat	188	$J\cdot kg^{-1}\cdot K^{-1}$
Simplified TEM	thermal conductivity	$-2.90574\times10^{-9}T^4+4.33411\times10^{-6}T^3$ $-0.00239T^2+0.57868T-51.05908$	$W\cdot m^{-1}\cdot K^{-1}$
	specific heat	485	$J\cdot kg^{-1}\cdot K^{-1}$

in which, t denotes the time, and ρ, $\vec{v}$, p, μ, T, λ, and c represent the density, velocity vector, pressure, dynamic viscosity, absolute temperature, thermal conductivity, and specific heat of fluids, respectively.

The flow pattern of exhaust gas and cooling water can be regarded as turbulent flow [39], and the standard k - ε model is used to solve the turbulence flow in this work, which transport equations include:

$$\frac{\partial}{\partial t}(\rho k)+\rho(\vec{v}\cdot\nabla)k=\nabla\cdot\left[\left(\mu+\frac{\mu_t}{\sigma_k}\right)\nabla k\right]+P_k-\rho\varepsilon \tag{4}$$

$$\frac{\partial}{\partial t}(\rho\varepsilon)+\rho(\vec{v}\cdot\nabla)\varepsilon=\nabla\cdot\left[\left(\mu+\frac{\mu_t}{\sigma_\varepsilon}\right)\nabla\varepsilon\right]+C_{1\varepsilon}\frac{\varepsilon}{k}P_k-C_{2\varepsilon}\rho\frac{\varepsilon^2}{k} \tag{5}$$

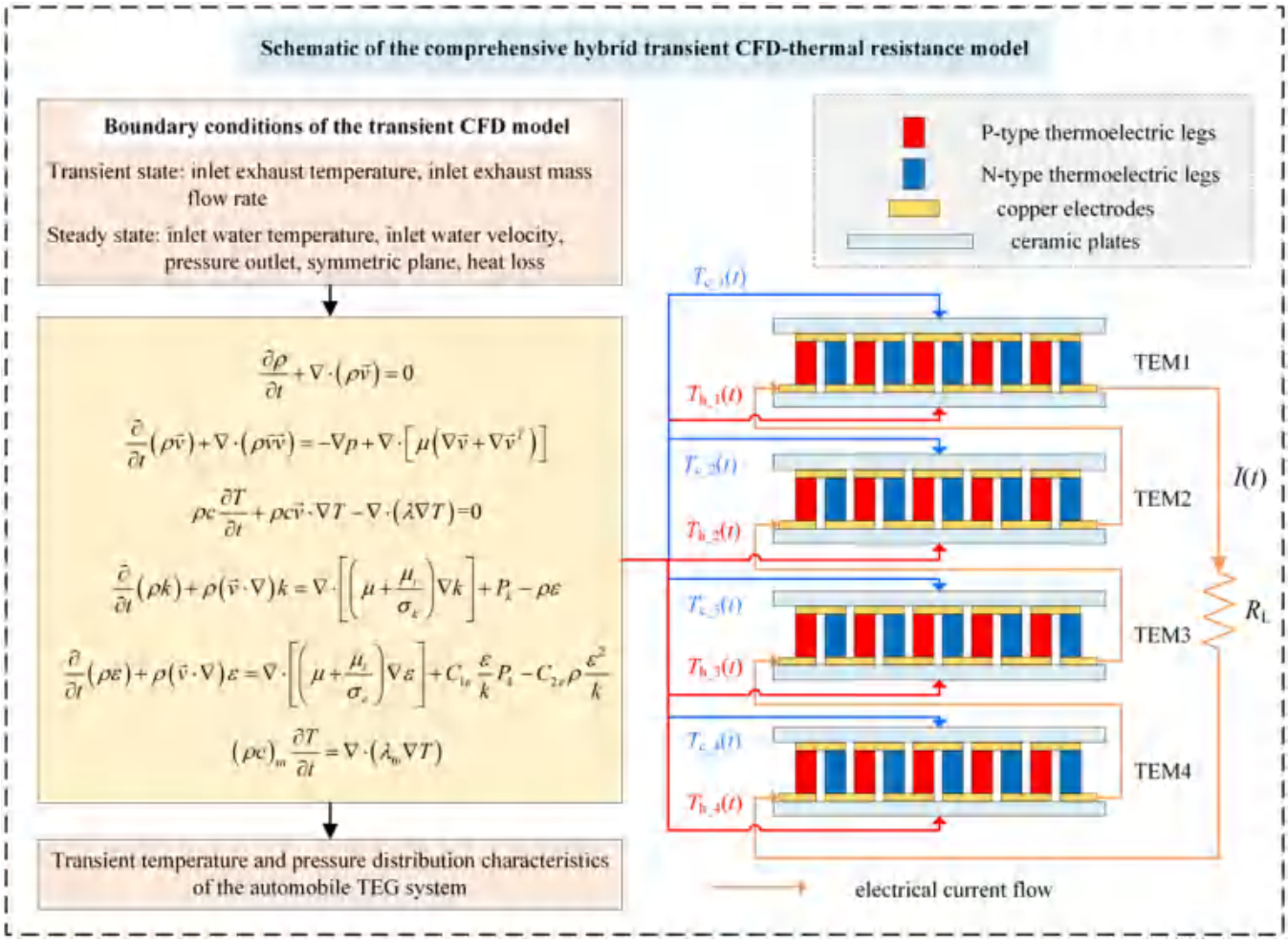

Fig. 2. Schematic of the comprehensive hybrid transient CFD-thermal resistance model.

with

$$\mu_t = \rho C_\mu \frac{k^2}{\varepsilon} \tag{6}$$

in which, k and ε represent the turbulence kinetic energy and its dissipation rate, respectively. P_k denotes the shear production of k. The model constants of $C_{1\varepsilon} = 1.44$, $C_{2\varepsilon} = 1.92$, $C_\mu = 0.09$, $\sigma_k = 1.0$, and $\sigma_\varepsilon = 1.3$ are referenced from [40].

The transient heat and mass transfer in fluid domains can be characterized by Eqs (1)–(6). In solid domains, transient energy conservation is defined as:

$$\rho c \frac{\partial T}{\partial t} = \nabla \cdot (\lambda \nabla T) \tag{7}$$

The heat loss is defined on the walls of the ATEG system exposed to surroundings, which is [41]:

$$-\lambda \frac{\partial T}{\partial n} = h_{en}(T - T_{en}) \tag{8}$$

in which, $h_{en} = 15\ \mathrm{W \cdot m^{-2} \cdot K^{-1}}$ and $T_{en} = 300$ K are the environmental heat transfer coefficient and environmental temperature [42], respectively.

In this work, the CFD simulation is carried out by using the COMSOL package. According to the CFD results, the transient mean surface temperature on the two sides of all TEMs is calculated and taken as temperature inputs of the transient thermal resistance model. Fig. 2 shows the schematic of the comprehensive hybrid transient CFD-thermal resistance model. Here, four TEMs in the 1/4 ATEG system are connected in series, thus, the electrical current passing through all TEMs is the same. The four TEMs along the direction of exhaust flow are labeled as TEM1, TEM2, TEM3, and TEM4 respectively.

For the transient thermal resistance model, the heat absorption on the hot sides of each TEM can be expressed as:

$$Q_{h\_i}(t) = \alpha_{pn\_i} I(t) T_{hleg\_i}(t) + \frac{T_{hleg\_i}(t) - T_{cleg\_i}(t)}{R_{leg\_i}} - \frac{1}{2} I^2(t) R_{in\_i} \tag{9}$$

in which, t is the time variable, α_{pn} represents the Seebeck coefficient of each TEM, I represents the electrical current, T_{hleg} and T_{cleg} are respectively the hot- and cold-side temperature of thermoelectric legs, R_{leg} represents the thermal resistance of thermoelectric legs, and R_{in} represents the internal resistance of each TEM. Subscripts $i = 1, 2, 3$, and 4 represent TEM1, TEM2, TEM3, and TEM4, respectively. It is worth noting that Eq. (9) includes four Equations.

Similarly, the heat dissipation on the cold side of each TEM can be written as:

$$Q_{c\_i}(t) = \alpha_{pn\_i} I(t) T_{cleg\_i}(t) + \frac{T_{hleg\_i}(t) - T_{cleg\_i}(t)}{R_{leg\_i}} + \frac{1}{2} I^2(t) R_{in\_i} \tag{10}$$

Here, the temperature dependence of thermoelectric materials is considered. Assuming that the working temperature of thermoelectric materials is equal to the mean temperature on both sides

of thermoelectric legs [43], α_{pn_i}, R_{leg_i}, and R_{in_i} can be derived by Eqs (11)–(13), respectively,

$$\alpha_{pn\_i} = N\left[\alpha_p\left(\bar{T}_i\right) - \alpha_n\left(\bar{T}_i\right)\right] \tag{11}$$

$$R_{leg\_i} = \frac{H_{leg}}{N\left(\lambda_p\left(\bar{T}_i\right) + \lambda_n\left(\bar{T}_i\right)\right)A_{leg}} \tag{12}$$

$$R_{in\_i} = N\left[\sigma_p^{-1}\left(\bar{T}_i\right) + \sigma_n^{-1}\left(\bar{T}_i\right)\right]\frac{H_{leg}}{A_{leg}} \tag{13}$$

with

$$\bar{T}_i = \frac{T_{hleg\_i} + T_{cleg\_i}}{2} \tag{14}$$

in which, N represents the number of p-type or n-type thermoelectric legs, α is the Seebeck coefficient, λ is the thermal conductivity, σ^{-1} is the electrical conductivity. H is the height, and A is the cross-sectional area, respectively. Subscripts leg, p, and n are respectively the thermoelectric leg, p-type thermoelectric leg, and n-type thermoelectric leg.

Also, the heat absorption on the hot side and heat dissipation can be written by:

$$Q_{h\_i}(t) = \frac{T_{h\_i}(t) - T_{hleg\_i}(t)}{R_h} \tag{15}$$

$$Q_{c\_i}(t) = \frac{T_{cleg\_i}(t) - T_{c\_i}(t)}{R_c} \tag{16}$$

with

$$R_h = R_{hce} + R_{co} = \frac{H_{hce}}{\lambda_{hce}A_{hce}} + \frac{H_{co}}{\lambda_{co}NA_{co}} \tag{17}$$

$$R_c = R_{cce} + R_{co} = \frac{H_{cce}}{\lambda_{cce}A_{cce}} + \frac{H_{co}}{\lambda_{co}NA_{co}} \tag{18}$$

in which, R_h and R_c are the hot- and cold-side thermal resistances from T_h and T_c to T_{hleg} and T_{cleg} respectively. Subscripts co, hce, and cce denote the copper conducting strips, the hot-side and cold-side ceramic plates.

Also, the electrical current flowing through all TEMs can be expressed by:

$$I(t) = \frac{\sum_{i=1}^{4}\alpha_{pn\_i}\left[T_{hleg\_i}(t) - T_{cleg\_i}(t)\right]}{\sum_{i=1}^{4}R_{in\_i} + R_L} \tag{19}$$

where R_L denotes the load resistance.

According to Eqs. (9), (10), (15), (16), and (19), there are 17 formulas with 17 unknowns of $Q_{h\_1}(t)$, $Q_{h\_2}(t)$, $Q_{h\_3}(t)$, $Q_{h\_4}(t)$, $Q_{c\_1}(t)$, $Q_{c\_2}(t)$, $Q_{c\_3}(t)$, $Q_{c\_4}(t)$, $T_{hleg\_1}(t)$, $T_{hleg\_2}(t)$, $T_{hleg\_3}(t)$, $T_{hleg\_4}(t)$, $T_{cleg\_1}(t)$, $T_{cleg\_2}(t)$, $T_{cleg\_3}(t)$, $T_{cleg\_4}(t)$, and $I(t)$. However, T_{hleg} and T_{cleg} are unknown at the beginning of the calculation, resulting in the unknowns of α_{pn_i}, R_{leg_i}, and R_{in_i}. To handle this issue, an iteration method is adopted to solve the seventeen unknowns, as shown in Fig. 3. In the first calculation, the hot- and cold-side temperatures of thermoelectric legs, T_{hleg_i} and T_{cleg_i}, are replaced by the boundary heat source and cooling source input temperatures, T_{h_i} and T_{c_i}, and then, the initial values of α_{pn_i}, R_{leg_i}, and R_{in_i} are obtained. Furthermore, the values of T_{hleg_i} and T_{cleg_i} are updated and returned to the loop until convergence is satisfied.

According to the calculated results, the transient output power of each TEM can be obtained by:

$$P_i(t) = \alpha_{pn\_i}I(t)\cdot\left[T_{hleg\_i}(t) - T_{cleg\_i}(t)\right] - I^2(t)R_{in\_i} \tag{20}$$

The transient output voltage of each TEM can also be obtained by:

$$U_{L\_i}(t) = \alpha_{pn\_i}\left[T_{hleg\_i}(t) - T_{cleg\_i}(t)\right] - I(t)R_{in\_i} \tag{21}$$

Therefore, the transient conversion efficiency of each TEM can be estimated by:

$$\eta_i(t) = \frac{P_i(t)}{Q_i(t)} \tag{22}$$

For the 1/4 ATEG system, its dynamic output power can be evaluated by:

$$P(t) = \sum_{i=1}^{4}P_i(t) \tag{23}$$

Also, the dynamic conversion efficiency of the ATEG system can be obtained by:

$$\eta(t) = \frac{P(t)}{c_{ex}\dot{m}_{ex}(t)\cdot\left[T_{exi}(t) - T_{exo}(t)\right]} \tag{24}$$

where $\dot{m}(t)$ represents the dynamic mass flow rate. Subscripts ex, exi, and exo represent the exhaust gas, exhaust inlet, and exhaust outlet, respectively.

3.2. Boundary conditions

As can be observed in Fig. 1, the transient boundary conditions of the CFD model are derived from time-dependant exhaust parameters, because the exhaust heat is sensitive to the automobile operation conditions. As mentioned in Section 2, the ATEG system is applied to harvest the exhaust heat from a heavy truck, and the vehicle model is established on the platform of ADVISOR. The heavy truck operates under the highway fuel economy test (HWFET) driving cycles. When the exhaust parameters reach equilibrium, that is about the 20th driving cycle, the corresponding exhaust data are extracted as the transient exhaust boundary conditions of the CFD model, as shown in Fig. 4. It should be noted that the mass flow was divided by 4 in Fig. 4, because the 1/4 ATEG system is used as the research objective in this work. The exhaust temperature shows a similar variation with the vehicle speed, whereas the mass flow fluctuates violently. Beside the transient boundary conditions, the steady-state ones of the CFD model include the pressure outlet of fluid regions, the inlet water temperature and velocity on the inlet surface of the coolant channel, the symmetrical boundary condition on the symmetric surfaces (see Fig. 1), and the heat loss as defined in Eq. (8). Details about the boundary conditions are listed in Table 2.

Regarding the transient thermal resistance model, its transient temperature boundary conditions are obtained from the CFD results, as shown in Fig. 2. The four TEMs are connected in series with a load resistor, and the load resistance is set as $R_L = 17\ \Omega$. Compared with the previous thermal resistance model used to calculate the output of a single TEM [44], this model takes into account the topological connection among TEMs. Beside, by altering the topological connection among TEMs, the influence of different connection modes on the output performance of the ATEG system is studied, including parallel and hybrid connection modes. For instance, when the four TEMs are connected in parallel, combined with Eqs. (9), (10) and (15), (16), there are 20 formulas with 20 unknowns in total, because Eq. (19) can be extended to four Equations according to the current relationship among TEMs. Through the same solving process as the transient thermal resistance model in Fig. 3, the dynamic outputs of TEMs in parallel can be calculated.

Compared with the dynamic model in Ref. [33], the developed in this work can simulate the complete geometric structure of automobile TEG systems with numerous TEMs, reduce the calculation time, and facilitate the study of the topological relationship between TEMs. Regarding the transient thermal resistance model, compared with the previous heat transfer analysis, this work extended the thermal resistance network from a steady state to a

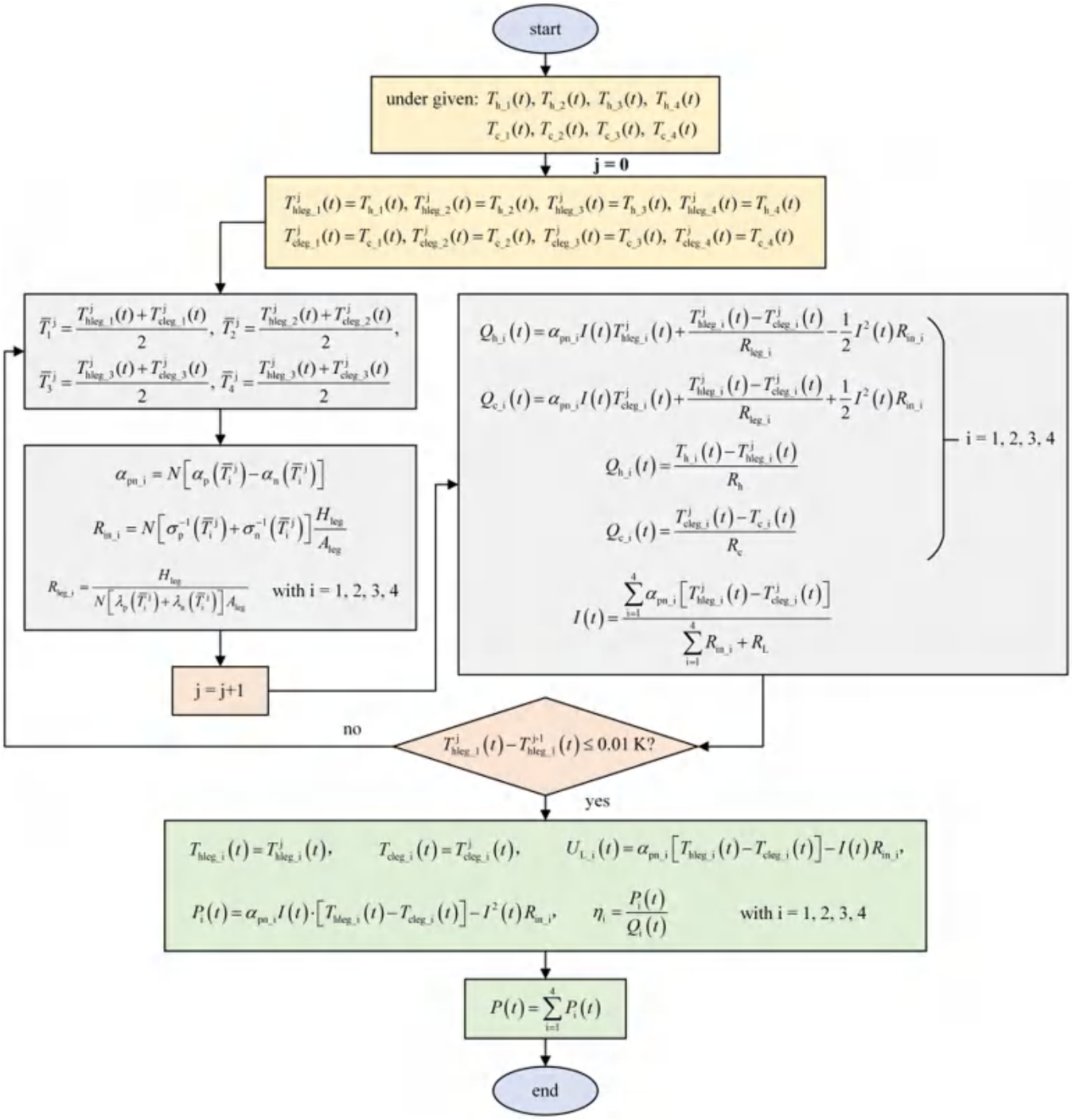

Fig. 3. Solution procedures of the transient thermal resistance model.

Table 2
Boundary conditions of the transient CFD model.

Name	Position	Steady or transient	Value	Unit
exhaust temperature	inlet surface of the exhaust channel	transient	$T_{ex}(t)$ in Fig. 4	K
exhaust mass flow rate	inlet surface of the exhaust channel	transient	$\dot{m}_{ex}(t)$ in Fig. 4	g/s
water temperature	inlet surface of the coolant channel	steady	363.15	K
water velocity	inlet surface of the coolant channel	steady	1	m/s
pressure outlet	outlet surfaces of the exhaust and coolant channels	steady	1	atm
symmetrical boundary	symmetric surfaces in Fig. 1	steady	NA	NA
heat loss	surfaces exposed to the environment	steady	Eq. (8)	NA

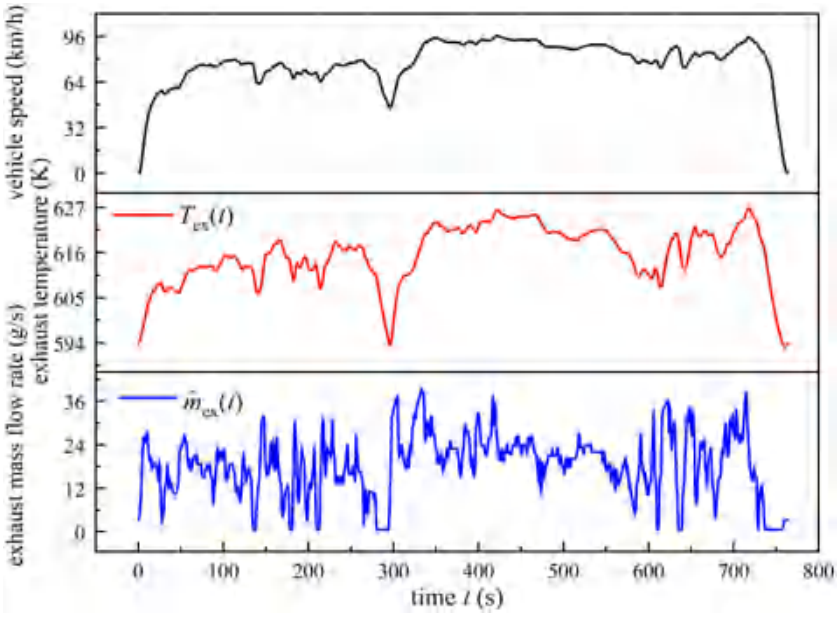

Fig. 4. Transient exhaust temperature and mass flow rate under the HWFET driving cycle.

transient state and from only one TEM to numerous TEMs. In addition, the topological connection among TEMs is considered through an iterative solution method via MATLAB, which is more applicable and in line with real situations.

3.3 Grid independence analysis

The transient CFD model is solved by the finite element method on the platform of COMSOL Multiphysics. It is necessary to check the grid convergence before carrying out transient CFD simulations, because the output of the ATEG system is sensitive to the grid parameters. Taking the mean exhaust temperature (615.46 K) and mass flow rate (18.26 g/s) as boundary conditions, the steady-state CFD simulation of the 1/4 ATEG system was carried out by using four grid strategies: 347,888 for the coarse grid, 751,672 for the standard grid, 1,268,538 for the fine grid, and 2,952,180 for the finer grid, respectively. The preliminary simulation results showed that the relatively small difference and short computing time in mean temperature were obtained between the standard and fine grids. Therefore, the grid strategy with 751,672 grid elements was selected for the following transient numerical calculations. During transient simulations, the time variable was discretized by the backward difference method, and an adaptive time step method with a maximum step size of 0.1 s was adopted. The workstation with 2 CPUs, 24 cores, and 256 G memory was used to carry out simulations.

4. Experimental validation

The prototype of the ATEG system was fabricated, as shown in Fig. 5(b), which features the same geometric and material parameters as described in Fig. 1. During the assembly process, the bakelite frames with eight holes were attached on both hot sides of the heat exchanger to fix eight TEMs. The whole structure was clamped by stainless bars. To ensure sufficient clamping force, the tightening torque was continuously applied to the cap screws until the output power of the ATEG system does not change. Also, to avoid the air gap caused by the flatness and assembly process, thermal grease was smeared on the contact interfaces between components.

The comprehensive hybrid transient CFD-thermal resistance model was verified experimentally through a designed transient experimental test bench, as shown in Fig. 5(a). To measure the dynamic performance of the ATEG system, an air heater (F1-R1055, FTV, China) was used to produce high-temperature dry air for the ATEG system. During the test, the air velocity and temperature change instantaneously by turning the temperature knob and flux knob on the heater. Two K-type temperature sensors (WRNT, Huarun, China) were inserted into the inlet and outlet of the ATEG system to test the transient inlet air temperature and outlet air temperature respectively. The transient temperature data were recorded and stored by a data logger (RDXL4SD, OMEGA, US). As in the simulation, four TEMs on the same side of the ATEG system were connected in series with an electronic load (IT8500+, ITECH, China), and the load resistance value is set as 17 Ω. However, the electronic load could not be used to measure and record the transient output voltage. Therefore, a voltage data logger (KSF, Keshun, China) was used to record the transient output voltage. To test the transient air velocity, a hot-wire anemometer (HHF-SD1, OMEGA, US) was placed behind the ATEG system, which is comprised of an air velocity data logger and an air velocity sensor. Nevertheless, the maximum operating temperature of the air velocity sensor is 50 °C, which is far lower than the air temperature. Therefore, an air cooler powered by a DC power supply (UTP1305, UNI-T, China) was configured between the ATEG system and the hot-wire anemometer to protect the air velocity sensor. For the cold side of the ATEG system, tap water with a mass flow rate of 21.19 g/s and a temperature of 284.85 K flows through heat sinks to provide a constant cooling source. The instrument accuracies of the voltage data logger, temperature data logger, and hot-wire anemometer are ±0.2%, ±0.4%, and ±5%, respectively.

According to experiments, the transient air velocity and temperature (see Fig. 5(c)) were measured and taken as the transient air boundary conditions. In this section, the transient air velocity boundary condition was used, instead of the mass flow rate, because only the velocity data can be obtained through the velocity sensor. Combined with the steady-state boundary conditions of cooling water, the corresponding model results were evaluated by the hybrid transient CFD-thermal resistance model. Fig. 5(d) illustrates the comparison of output power and outlet air temperature

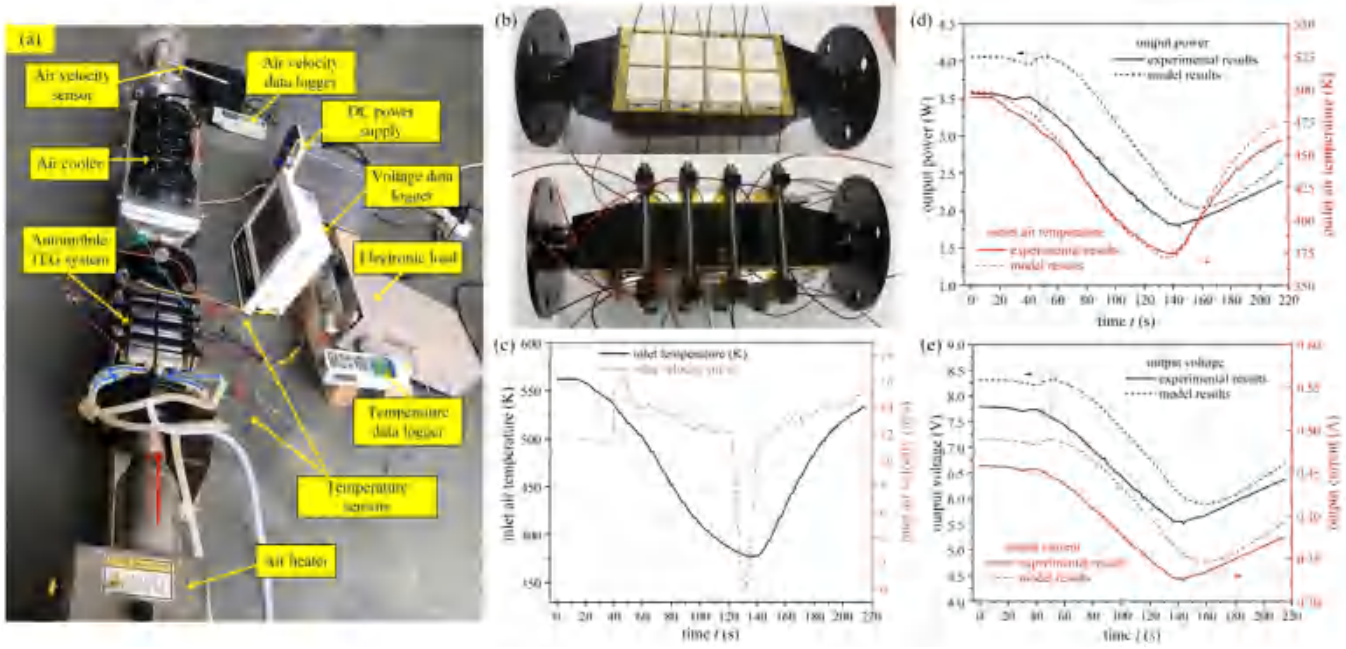

Fig. 5. Transient experimental validations. (a) Transient experimental test bench. (b) Prototype of the ATEG system. (c) Transient inlet air boundary conditions of the transient CFD model obtained from experiments. (d) Comparison of output power and outlet air temperature between model and experimental results. (e) Comparison of output voltage and current between model and experimental results.

between the model and test results. The variation of output power and outlet air temperature predicted by the model shows a similar trend as experimental results. However, the output power predicted by the model is 14.67% average higher than that of experiments, which is mainly caused by the instrument errors, such as data loggers and hot-wire anemometer, followed by the neglect of thermal grease in simulations. Also, taking the output power as the criterion further amplifies the error, because the power is proportional to the square of the temperature difference of TEMs. For the outlet air temperature, the mean error between experimental and model results is 1.12%, which indicates that the transient model is highly reasonable. Fig. 5(e) illustrates the comparison of voltage and current between the model and test results. The mean error of voltage between predictions and experiments is the same as that of output current, and that is about 7.70%. It can also be observed from the figure that the model results have a greater response hysteresis than experimental results because of the signal delay of air temperature and velocity sensors, and the delayed signal is recorded and used for numerical calculations.

5. Dynamic performance of the automobile thermoelectric generator system

5.1. Transient temperature distribution of the ATEG system

Fig. 6 shows temperature distributions of the ATEG system solved by the transient CFD model at t = 200 s, 400 s, and 600 s. When t = 200 s, 400 s, and 600 s, the inlet exhaust temperatures are 612.12 K, 622.24 K, and 610.61 K respectively, and the inlet exhaust mass flow rates are 10.13 g/s, 32.89 g/s, and 10.17 g/s respectively. It can be observed from Fig. 6(a) that the wall temperature of the heat exchanger at t = 400 s shows the highest value due to the largest exhaust mass flow rate and temperature. Although the exhaust temperature at t = 200 s is relatively higher than that at t = 600 s and the exhaust mass flow rate is the almost same, the surface temperature of the heat exchanger when t = 600 s is much higher than that when t = 200 s, which can be attributed to the thermal inertia. According to Fig. 4, when t = 600 s, the exhaust temperature decreases from a high level to a low level, however, due to the influence of thermal inertia, the temperature does not respond immediately and remains in its previous state for a short time, thus resulting in a higher temperature. In addition, a temperature drop can be observed from the exhaust inlet to the exhaust outlet, causing the uneven output of different TEMs. Optimizing the topological connection among TEMs [45] is an effective approach to diminish the negative effect caused by this uneven output. Compared with previous models, this model takes into account the topological connection of TEMs, which can provide a guide on how to connect TEMs more effectively.

Fig. 6(b) shows the temperature distribution of TEMs. The same phenomenon in Fig. 6(a) can be observed more clearly here. Based on temperature distributions, the mean hot- and cold-side temperatures of TEMs can be obtained. For instance, when t = 400 s, the mean hot (cold) side temperatures of TEM1, TEM2, TEM3, and TEM4 are 512.56 K (371.18 K), 501.95 K (371.11 K), 497.38 K (370.92 K), and 499.37 K (370.69 K), respectively. The main purpose of the transient mean hot- and cold-side temperatures of TEMs is to be used as temperature boundary conditions of the transient thermal resistance model, and then the dynamic behaviour of the ATEG system can be worked out.

Fig. 7(a) and (b) show the transient hot- and cold-side mean temperatures of TEMs respectively. The temperature difference between different TEMs on the cold side is less than that on the hot side, because the specific heat of cooling water is greater than that of dry air, and the temperature rise from the water inlet to the water outlet is lower than the temperature drop from the exhaust inlet to the exhaust outlet. Combined with Fig. 4, the variation of hot-side temperature is roughly consistent with the variation of exhaust temperature and is slightly affected by the exhaust mass flow rate. Also, the hot-side temperature of TEM4 is slightly greater than that of TEM3 because of the reverse flow of the exhaust gas near the outlet of the heat exchanger, as shown in Fig. 7(c). The transient hot- and cold-side temperatures in Fig. 7 are imported into the transient thermal resistance model, and the dynamic be-

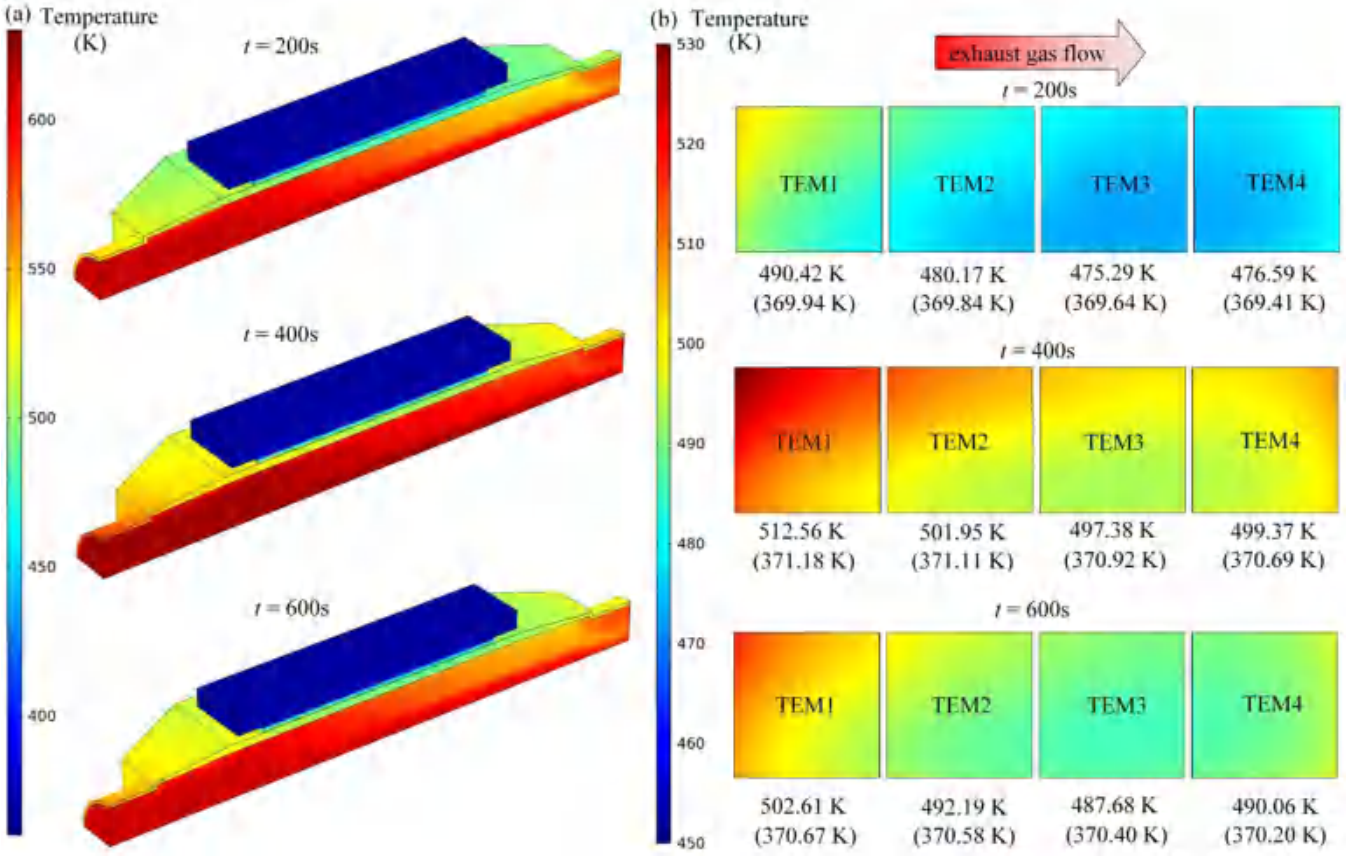

Fig. 6. Temperature distribution of the ATEG system at different time points. (a) The whole ATEG system. (b) TEMs.

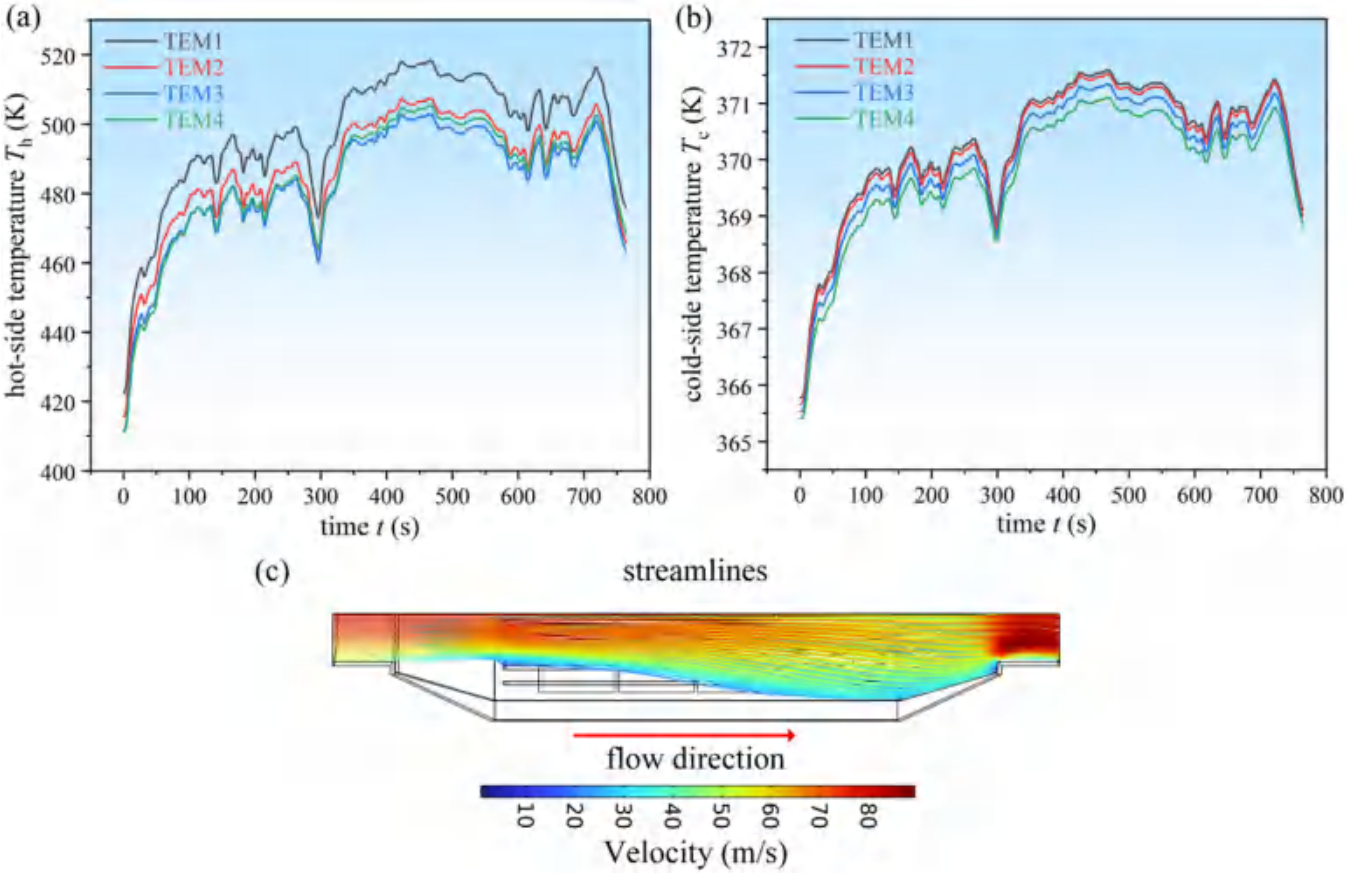

Fig. 7. Transient hot- and cold-side temperature of TEMs. (a) Hot-side temperature of TEMs. (b) Cold-side temperature of TEMs. (c) Streamlines.

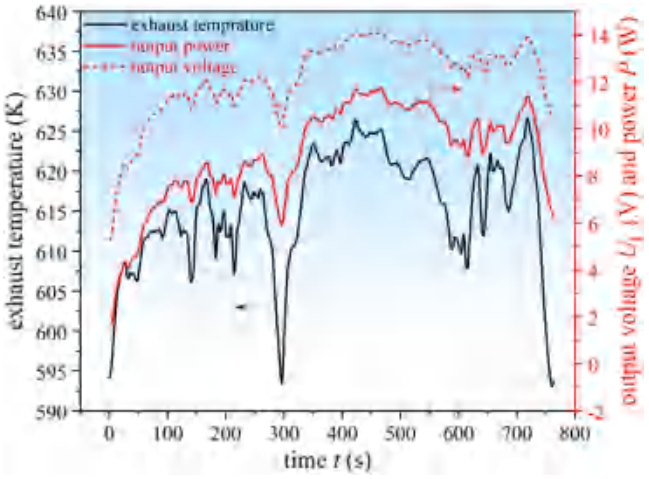

Fig. 8. Dynamic output voltage and power of the ATEG system.

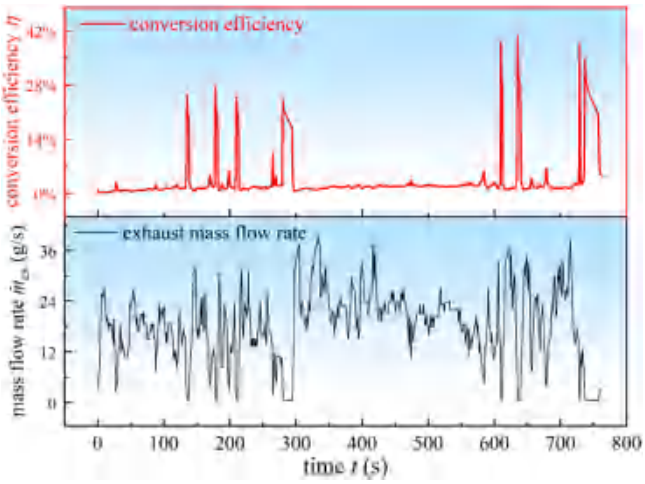

Fig. 9. Dynamic response characteristics on the conversion efficiency of the ATEG system.

haviour of the ATEG system is solved by the iterative method in Fig. 3 through MATLAB.

5.2. Dynamic behaviour of the ATEG system

Fig. 8 illustrates the dynamic output voltage and power of the ATEG system. The output power is directly proportional to the square of the output voltage, which leads to a greater fluctuation of the output power than the output voltage. Compared with the exhaust temperature, the output power and voltage present a more stable variation, because there is thermal buffering when heat is transferred from both sides of the TEM to the thermoelectric legs [46]. When $t = 466$ s, the output power of the ATEG system reaches the highest value of 11.73 W. In this study, the 1/4 ATEG system is used as the research object, and thus, the maximum power of the whole ATEG system is 46.92 W. Under the whole HWFET driving cycle, the mean power of the ATEG system is 8.91 W, which is 8.53% lower than the 9.67 W predicted by the steady-state hybrid CFD-thermal resistance model with the mean exhaust mass flow rate and temperature as boundary conditions. Consequently, the steady-state performance analysis of the ATEG system based on the mean exhaust parameters may overestimate the output power, and it is more reasonable to study its dynamic behaviour through a transient model.

The conversion efficiency of the ATEG system is an essential index to assess its application prospects. In the previous steady-state studies [47,48], the overall conversion efficiency of the ATEG system is around 2%. The ATEG system will be attractive and widely used in automobiles if its conversion efficiency can exceed 10%. Fig. 9 illustrates the dynamic response characteristics of the conversion efficiency of the ATEG system. According to Eq. (24), the conversion efficiency of the ATEG system is inversely proportional to the exhaust mass flow. When the vehicle is in an idle state, the exhaust flow rate will be at a relatively low level, nevertheless, the temperature of TEMs will not decrease instantly and continue to work due to the thermal inertia, thus resulting in dramatically high efficiency of the ATEG system. The maximum conversion efficiency of the ATEG system is 40.88%. However, it makes no sense to use an instantaneous value to estimate the conversion efficiency of the ATEG system. Under the whole HWFET driving cycle, the mean conversion efficiency of the ATEG system is 3.39%, which is 47.52% higher than the conversion efficiency of 1.78% expected from a steady-state analysis. Therefore, the steady-state model may significantly underestimate the conversion efficiency of the ATEG system.

5.3. Dynamic output performance of TEMs

Fig. 10(a) shows the dynamic output power of different TEMs. The overall power of four TEMs can be regarded as the output power of the ATEG system, and the variation in the power of the TEM presents the same trend as that of the ATEG system. However, the output power of different TEMs varies greatly, i.e., the mean output powers of TEM1, TEM2, TEM3, and TEM4 are respectively 2.57 W, 2.20 W, 2.04 W, and 2.10 W under the whole HWFET driving cycle, which is attributed to the uneven temperature distributions and the temperature drop from the exhaust inlet to the exhaust outlet. Herein, four TEMs are connected in series, resulting in parasitic loss because the overall output current of the ATEG system is limited by the minimum one of the TEMs. Accordingly, the output power of the ATEG system can be improved by optimizing the topological connection of TEMs, and it is investigated in the following section.

The dynamic conversion efficiency of TEMs differes from that of the ATEG system, because the conversion efficiency of TEMs is calculated based on the heat extracted from the heat exchanger rather than the heat extracted from the exhaust gas, as expressed in Eq. (22). Fig. 10(b) gives the dynamic conversion efficiency of different TEMs. The variation of TEM conversion efficiency shows a similar trend as that of output power, because the TEM conversion efficiency depends on its output power and hot-side temperature, while both have the same changing trend. Under the whole HWFET driving cycle, the mean conversion efficiencies of TEM1, TEM2, TEM3, and TEM4 are 1.82%, 1.70%, 1.64%, and 1.67%, respectively. It can be concluded that the ATEG system can reach a higher conversion efficiency than that of TEM itself when it is used to recover the dynamic automobile exhaust heat.

5.4. Effect of the topological connection on the performance of the ATEG system

In this section, the effect of the topological connection on the performance of the ATEG system is investigated. Fig. 11 shows the different topological connections among TEMs: (i) In case1, four TEMs are connected in series; (ii) In case2, four TEMs are connected in parallel; (iii) In case3, TEM1 and TEM3 are connected in series, TEM2 and TEM4 are connected in series, and then the two are connected in parallel; (iv) In case4, TEM1 and TEM4 are connected in series, TEM2 and TEM3 are connected in series, and then the two are connected in parallel. When the output current of each TEM is close, the series connection can achieve the highest perfor-

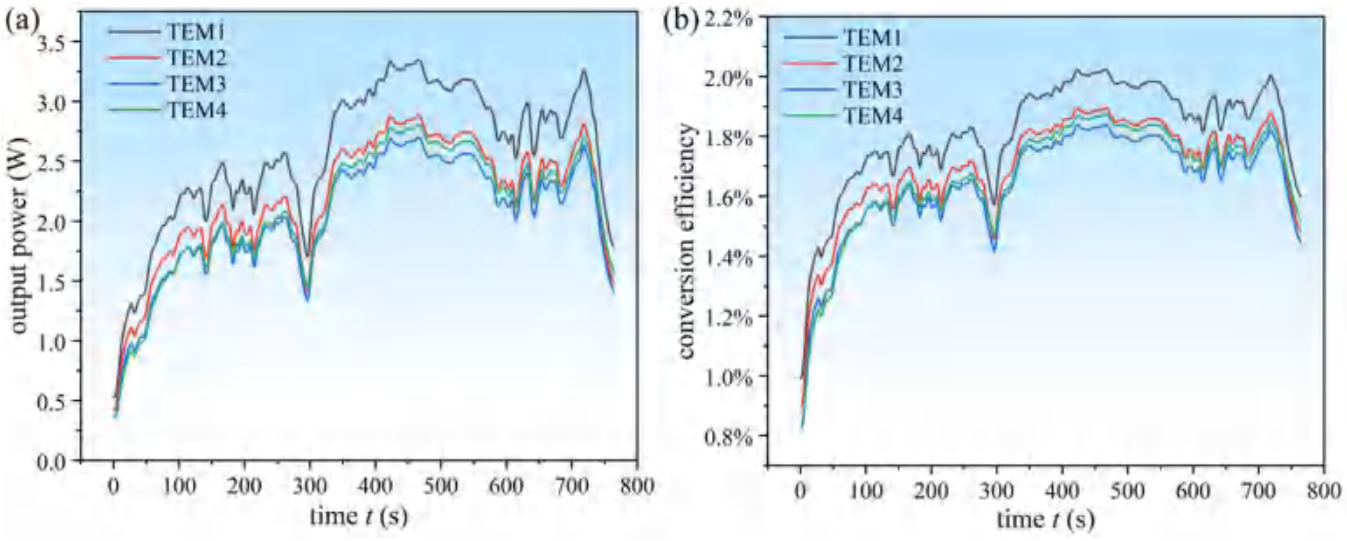

Fig. 10. Dynamic output power and conversion efficiency of different TEMs. (a) Output power. (b) Conversion efficiency.

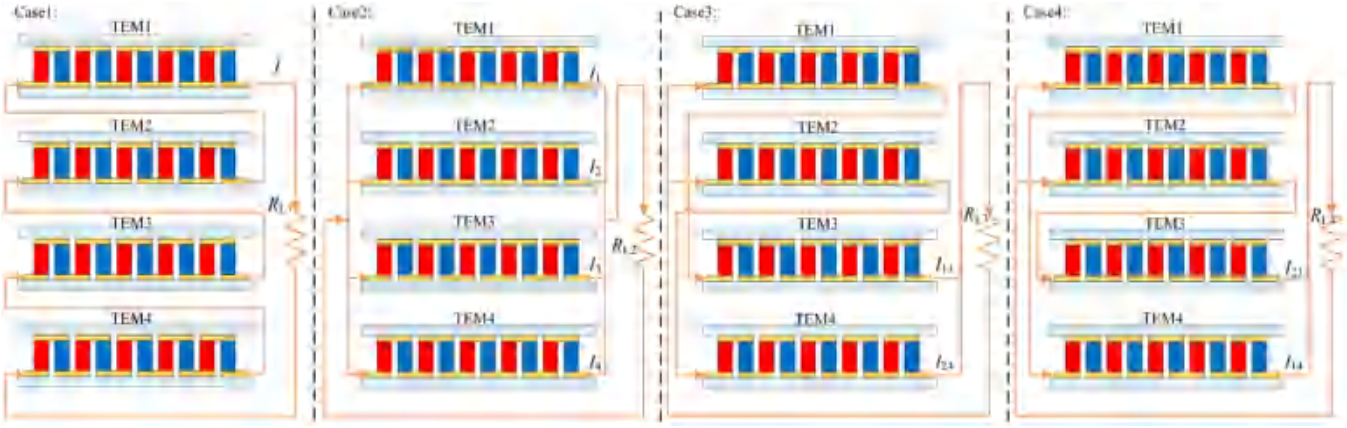

Fig. 11. Different topological connections among TEMs.

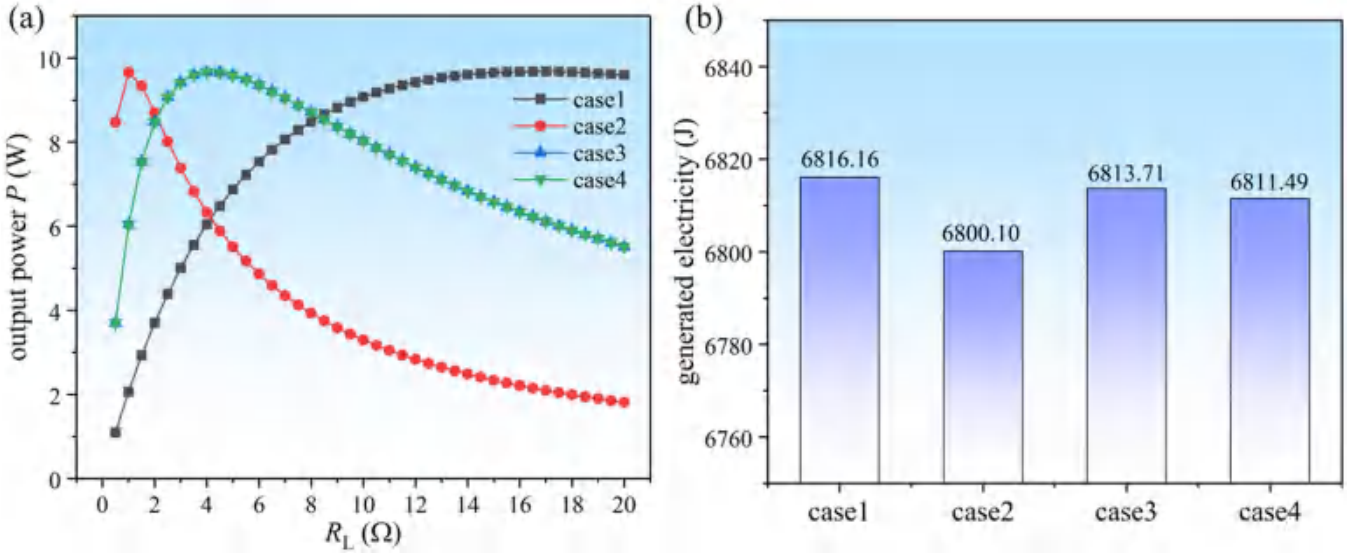

Fig. 12. The effect of the topological connection among TEMs on the output performance of the ATEG system. (a) Output power under different load resistances. (b) Generated electricity under the whole HWFET driving cycle.

mance; When the output voltage of each TEM is close, the parallel connection can achieve the highest performance; Otherwise, the hybrid connection may achieve the highest performance by optimizing the number of TEMs in series and parallel according to its specific output current and voltage. In different cases, the optimal load resistance is different. Therefore, the optimal load resistance under four cases is determined by the steady-state analysis, and then the total power generation of the ATEG system under four cases estimated by the transient model is compared.

Fig. 12(a) shows the relationship between output power and load resistance of the ATEG system in four cases. It can be seen that the optimal load resistance in case1 is the largest, because the internal resistance in the circuit is the sum of the four TEM internal resistances. With the optimal resistance, the steady-state output power of the ATEG system is 9.675 W, 9.652 W, 9.669 W, and 9.665 W under case1, case2, case3, and case4, respectively. Fig. 12(b) shows the generated electricity of the ATEG system over the whole HWFET driving cycle. Here, the required time of an HWFET driving cycle is 765 s. Similarly, the electricity produced by the ATEG system under case1 is the highest, followed by case3, case4, and case2. The reason why the series connection of TEMs can produce the highest power generation is that the parasitic loss caused by the difference in output current is lower than that caused by the difference in output voltage. In theory, the hybrid connection of TEMs can reach the highest output performance. However, in this study, only the 1/4 ATEG system with four TEMs is taken as the research objective. The number of TEMs is too small to give full play to the advantages of the hybrid connection. The more TEMs used in the ATEG system, the greater influence of the topological connection is, and the greater gains of the hybrid connection will be.

6. Conclusions

In this study, a comprehensive hybrid transient CFD-thermal resistance model is established to evaluate the dynamic behaviour of an ATEG system, with the consideration of the temperature dependences, the topological connection of TEMs, and the transient heat and mass transfer. Considering that the geometry of the ATEG system is completely symmetrical, only 1/4 of the structure is used as the research objective to reduce the workload. Taking the transient exhaust heat of a heavy truck running in an HWFET driving cycle as the heat source inputs of the transient model, the dynamic behaviour of the ATEG system is obtained and analyzed in detail. Beside, the transient CFD-thermal resistance model is validated experimentally through a transient performance test rig. Finally, the effect of the topology relationship among TEMs on the performance of the ATEG system is investigated by adjusting the conservation equations of the transient thermal resistance model. The main findings are drawn as follows:

(1) The comprehensive hybrid transient CFD-thermal resistance model can fully utilize the advantages of the numerical model and thermal resistance model, which can be used to predict the dynamic behaviour of the ATEG system with high accuracy and a short computational time. By comparing the experimental results with the model results, it can be obtained that the mean deviations of the output voltage and outlet air temperature are 7.70% and 1.12% respectively.
(2) Different from the steady-state results, under transient conditions, the hot-side temperature and output performance of TEMs at a certain time point with a high-level exhaust heat may be lower than that at a certain time point with a low-level exhaust heat, which is caused by the thermal inertia, that is, the hot-side temperature will not respond instantly with the variation of exhaust parameters.
(3) The dynamic output power of the ATEG system is mainly related to the exhaust temperature, but the variation of output power is more stable than that of exhaust temperature because of the thermal buffering as heat is transferred from the exhaust gas to TEMs. The dynamic conversion efficiency of the ATEG system is mainly dependant on the exhaust mass flow rate, and the instantaneous conversion efficiency can reach an ultra-high value when the vehicle is in an idle state owing to the effect of thermal inertia.
(4) According to the dynamic output performance evaluated by the proposed transient model, the mean output power and conversion efficiency of the ATEG system under the whole HWFET driving cycle are 8.91 W and 3.39% respectively. Combined with the results evaluated by the steady-state model using the mean exhaust mass flow rate and temperature as boundary conditions, the steady-state model overestimates the output power by 8.53% and underestimates the conversion efficiency by 47.52%.
(5) The output power of TEMs shows a similar variation to that of the ATEG system, whereas the conversion efficiency of TEMs quite differs from that of the ATEG system, because the TEM extracts heat from the heat exchanger rather than the exhaust gas. Due to the uneven hot-side temperature distribution of the heat exchanger, the output of TEMs varies greatly, resulting in a parasitic loss. Optimizing the topology of TEMs is one of the effective ways to reduce parasitic loss. The proposed model is convenient to evaluate the behaviour of the ATEG system with different topological connections of TEMs.

Declaration of Competing Interest

The authors declare that they have no known competing financial interests or personal relationships that could have appeared to influence the work reported in this paper.

CRediT authorship contribution statement

Ding Luo: Conceptualization, Methodology, Writing – original draft. **Yuying Yan:** Supervision. **Wei-Hsin Chen:** Writing – review & editing. **Xuelin Yang:** Funding acquisition. **Hao Chen:** Data curation. **Bingyang Cao:** Software, Writing – review & editing. **Yulong Zhao:** Investigation, Writing – review & editing.

Data availability

Data will be made available on request.

Acknowledgments

This work was supported by the National Natural Science Foundation of China (52072217, and 22179071), the Hubei Natural Science Foundation Innovation Group Project (2022CFA020), Joint Funds of the Hubei Natural Science Foundation Innovation and Development (2022CFD034).

References

[1] R. Saidur, M. Rezaei, W.K. Muzammil, M.H. Hassan, S. Paria, M. Hasanuzzaman, Technologies to recover exhaust heat from internal combustion engines, Renew. Sustain. Energy Rev. 16 (2012) 5649–5659.
[2] Z.G. Shen, L.L. Tian, X. Liu, Automotive exhaust thermoelectric generators: current status, challenges and future prospects, Energy Convers. Manag. 195 (2019) 1138–1173.
[3] M. Ge, Z. Li, Y. Zhao, Z. Xuan, Y. Li, Y Zhao, Experimental study of thermoelectric generator with different numbers of modules for waste heat recovery, Appl. Energy 322 (2022) 119523.
[4] S. Lan, R. Stobart, R. Chen, Performance comparison of a thermoelectric generator applied in conventional vehicles and extended-range electric vehicles, Energy Convers. Manag. 266 (2022) 115791.

[5] Y. Zhao, M. Lu, Y. Li, Y. Wang, M. Ge, Numerical investigation of an exhaust thermoelectric generator with a perforated plate, Energy 263 (2023) 125776.
[6] S. Shittu, G. Li, X. Zhao, X. Ma, Y.G. Akhlaghi, E. Ayodele, High performance and thermal stress analysis of a segmented annular thermoelectric generator, Energy Convers. Manag. 184 (2019) 180–193.
[7] W.H. Chen, Y.X. Lin, Y.B. Chiou, Y.L. Lin, X.D. Wang, A computational fluid dynamics (CFD) approach of thermoelectric generator (TEG) for power generation, Appl. Therm. Eng. 173 (2020) 115203.
[8] S.A. Mostafavi, M. Mahmoudi, Modeling and fabricating a prototype of a thermoelectric generator system of heat energy recovery from hot exhaust gases and evaluating the effects of important system parameters, Appl. Therm. Eng. 132 (2018) 624–636.
[9] D. Luo, Z. Sun, R. Wang, Performance investigation of a thermoelectric generator system applied in automobile exhaust waste heat recovery, Energy 238 (2022) 121816.
[10] P. Fernández-Yañez, O. Armas, A. Capetillo, S. Martínez-Martínez, Thermal analysis of a thermoelectric generator for light-duty diesel engines, Appl. Energy 226 (2018) 690–702.
[11] G. Zhang, K. Jiao, Z. Niu, H. Diao, Q. Du, H. Tian, et al., Power and efficiency factors for comprehensive evaluation of thermoelectric generator materials, Int. J. Heat Mass Transf. 93 (2016) 1034–1037.
[12] D. Luo, R. Wang, W. Yu, W. Zhou, A numerical study on the performance of a converging thermoelectric generator system used for waste heat recovery, Appl. Energy 270 (2020) 115181.
[13] T. Ma, X. Lu, J. Pandit, S.V. Ekkad, S.T. Huxtable, S. Deshpande, et al., Numerical study on thermoelectric–hydraulic performance of a thermoelectric power generator with a plate-fin heat exchanger with longitudinal vortex generators, Appl. Energy 185 (2017) 1343–1354.
[14] Y. Wang, S. Li, Y. Zhang, X. Yang, Y. Deng, C. Su, The influence of inner topology of exhaust heat exchanger and thermoelectric module distribution on the performance of automotive thermoelectric generator, Energy Convers. Manag. 126 (2016) 266–277.
[15] K. Nithyanandam, R.L. Mahajan, Evaluation of metal foam based thermoelectric generators for automobile waste heat recovery, Int. J. Heat Mass Transfer 122 (2018) 877–883.
[16] C.C. Weng, M.J. Huang, A simulation study of automotive waste heat recovery using a thermoelectric power generator, Int. J. Therm. Sci. 71 (2013) 302–309.
[17] C.T. Hsu, G.Y. Huang, H.S. Chu, B. Yu, D.J. Yao, Experiments and simulations on low-temperature waste heat harvesting system by thermoelectric power generators, Appl. Energy 88 (2011) 1291–1297.
[18] W. Li, J. Peng, W. Xiao, H. Wang, J. Zeng, J. Xie, et al., The temperature distribution and electrical performance of fluid heat exchanger-based thermoelectric generator, Appl. Therm. Eng. 118 (2017) 742–747.
[19] M. Keshtkar, M. Eslami, K. Jafarpur, Effect of design parameters on performance of passive basin solar stills considering instantaneous ambient conditions: a transient CFD modeling, Sol. Energy 201 (2020) 884–907.
[20] R. Scharler, T. Gruber, A. Ehrenhöfer, J. Kelz, R.M. Bardar, T. Bauer, et al., Transient CFD simulation of wood log combustion in stoves, Renew. Energy 145 (2020) 651–662.
[21] A. Papukchiev, D. Grishchenko, P. Kudinov, On the need for conjugate heat transfer modeling in transient CFD simulations, Nucl. Eng. Des. 367 (2020) 110796.
[22] X. Liu, C.-.F. Zhang, J.-.G. Zhou, X. Xiong, Y..P. Wang, Thermal performance of battery thermal management system using fins to enhance the combination of thermoelectric Cooler and phase change Material, Appl. Energy 322 (2022) 119503.
[23] H. Zhang, H. Xu, B. Chen, F. Dong, M Ni, Two-stage thermoelectric generators for waste heat recovery from solid oxide fuel cells, Energy 132 (2017) 280–288.
[24] X. Liang, X. Sun, H. Tian, G. Shu, Y. Wang, X. Wang, Comparison and parameter optimization of a two-stage thermoelectric generator using high temperature exhaust of internal combustion engine, Appl. Energy 130 (2014) 190–199.
[25] G. Fraisse, J. Ramousse, D. Sgorlon, C. Goupil, Comparison of different modeling approaches for thermoelectric elements, Energy Convers. Manag. 65 (2013) 351–356.
[26] A. Marvão, P.J. Coelho, H.C. Rodrigues, Optimization of a thermoelectric generator for heavy-duty vehicles, Energy Convers. Manag. 179 (2019) 178–191.
[27] S. Vale, L. Heber, P.J. Coelho, C.M. Silva, Parametric study of a thermoelectric generator system for exhaust gas energy recovery in diesel road freight transportation, Energy Convers. Manag. 133 (2017) 167–177.
[28] X. Gou, S. Yang, H. Xiao, Q Ou, A dynamic model for thermoelectric generator applied in waste heat recovery, Energy 52 (2013) 201–209.
[29] S. Lan, Z. Yang, R. Chen, R. Stobart, A dynamic model for thermoelectric generator applied to vehicle waste heat recovery, Appl. Energy 210 (2018) 327–338.
[30] D. Luo, Y. Zhao, Y. Yan, H. Chen, W.-.H. Chen, R. Wang, et al., Development of two transient models for predicting dynamic response characteristics of an automobile thermoelectric generator system, Appl. Therm. Eng. 221 (2023) 119793.
[31] S.R. Yan, H. Moria, S. Asaadi, H. Sadighi Dizaji, S. Khalilarya, K Jermsittiparsert, Performance and profit analysis of thermoelectric power generators mounted on channels with different cross-sectional shapes, Appl. Therm. Eng. (2020) 115455.
[32] D. Luo, R. Wang, W. Yu, W. Zhou, A novel optimization method for thermoelectric module used in waste heat recovery, Energy Convers. Manag. 209 (2020) 112645.
[33] D. Luo, R. Wang, Y. Yan, W. Yu, W. Zhou, Transient numerical modelling of a thermoelectric generator system used for automotive exhaust waste heat recovery, Appl. Energy 297 (2021) 117151.
[34] G.Y. Huang, C.T. Hsu, C.J. Fang, D.J. Yao, Optimization of a waste heat recovery system with thermoelectric generators by three-dimensional thermal resistance analysis, Energy Convers. Manag. 126 (2016) 581–594.
[35] D. Ji, S. Hu, Y. Feng, J. Qin, Z. Yin, A. Romagnoli, et al., Geometry optimization of solar thermoelectric generator under different operating conditions via Taguchi method, Energy Convers. Manag. 238 (2021) 114158.
[36] D. Luo, Z. Liu, Y. Yan, Y. Li, R. Wang, L. Zhang, et al., Recent advances in modeling and simulation of thermoelectric power generation, Energy Convers. Manag. 273 (2022) 116389.
[37] D. Luo, R. Wang, Experimental test and estimation of the equivalent thermoelectric properties for a thermoelectric module, J. Energy Res. Technol. 143 (2021) 122102.
[38] Y. Zhao, S. Wang, M. Ge, Z. Liang, Y. Liang, Y. Li, Performance investigation of an intermediate fluid thermoelectric generator for automobile exhaust waste heat recovery, Appl. Energy 239 (2019) 425–433.
[39] Y. Wang, S. Li, X. Xie, Y. Deng, X. Liu, C. Su, Performance evaluation of an automotive thermoelectric generator with inserted fins or dimpled-surface hot heat exchanger, Appl. Energy 218 (2018) 391–401.
[40] Fluent A. Fluent 14.0 user's guide 2011.
[41] Z. Miao, X. Meng, L. Liu, Analyzing and optimizing the power generation performance of thermoelectric generators based on an industrial environment, J. Power Sources 541 (2022) 231699.
[42] X. Liu, Y. Deng, K. Zhang, M. Xu, Y. Xu, C. Su, Experiments and simulations on heat exchangers in thermoelectric generator for automotive application, Appl. Therm. Eng. 71 (2014) 364–370.
[43] X.C. Xuan, K.C. Ng, C. Yap, H.T. Chua, The maximum temperature difference and polar characteristic of two-stage thermoelectric coolers, Cryogenics 42 (2002) 273–278.
[44] H. Cai, Z. Ye, G. Liu, A. Romagnoli, D. Ji, Sizing optimization of thermoelectric generator for low-grade thermal energy utilization: module level and system level, Appl. Therm. Eng. 221 (2023) 119823.
[45] R. Quan, X. Tang, S. Quan, L. Huang, A novel optimization method for the electric topology of thermoelectric modules used in an automobile exhaust thermoelectric generator, J. Electron. Mater. 42 (2012) 1469–1475.
[46] D. Luo, Y. Yan, Y. Li, R. Wang, S. Cheng, X. Yang, et al., A hybrid transient CFD-thermoelectric numerical model for automobile thermoelectric generator systems, Appl. Energy 332 (2023) 120502.
[47] T.Y. Kim, J. Kwak, B-w. Kim, Energy harvesting performance of hexagonal shaped thermoelectric generator for passenger vehicle applications: an experimental approach, Energy Convers. Manag. 160 (2018) 14–21.
[48] A. Ziolkowski, Automotive thermoelectric generator impact on the efficiency of a drive system with a combustion engine, MATEC Web Conf. 118 (2017).